University Library

MINERVA ACCESS

A gateway to Melbourne's research publications

Minerva Access is the Institutional Repository of The University of Melbourne

Author/s:
Robertson, IO;Scholten, SC;Singh, P;Healey, AJ;Meneses, F;Reineck, P;Abe, H;Ohshima, T;Kianinia, M;Aharonovich, I;Tetienne, J-P

Title:
Detection of Paramagnetic Spins with an Ultrathin van der Waals Quantum Sensor

Date:
2023-07-05

Citation:
Robertson, I. O., Scholten, S. C., Singh, P., Healey, A. J., Meneses, F., Reineck, P., Abe, H., Ohshima, T., Kianinia, M., Aharonovich, I. & Tetienne, J. -P. (2023). Detection of Paramagnetic Spins with an Ultrathin van der Waals Quantum Sensor. ACS Nano, 17 (14), pp.13408-13417. https://doi.org/10.1021/acsnano.3c01678.

Persistent Link:
https://hdl.handle.net/11343/337193

Detection of paramagnetic spins with an ultrathin van der Waals quantum sensor

Islay O. Robertson,[†] Sam C. Scholten,[‡,¶] Priya Singh,[†] Alexander J. Healey,[‡,¶,†]
Fernando Meneses,[‡,¶] Philipp Reineck,[†] Hiroshi Abe,[§] Takeshi Ohshima,[§]
Mehran Kianinia,[‖,⊥] Igor Aharonovich,[‖,⊥] and Jean-Philippe Tetienne[*,†]

†*School of Science, RMIT University, Melbourne, VIC 3001, Australia*
‡*School of Physics, University of Melbourne, VIC 3010, Australia*
¶*Centre for Quantum Computation and Communication Technology, School of Physics, University of Melbourne, VIC 3010, Australia*
§*National Institutes for Quantum Science and Technology (QST), 1233 Watanuki, Takasaki, Gunma 370-1292, Japan*
‖*School of Mathematical and Physical Sciences, University of Technology Sydney, Ultimo, NSW 2007, Australia*
⊥*ARC Centre of Excellence for Transformative Meta-Optical Systems, University of Technology Sydney, Ultimo, NSW 2007, Australia*

E-mail: jean-philippe.tetienne@rmit.edu.au

Abstract

Detecting magnetic noise from small quantities of paramagnetic spins is a powerful capability for chemical, biochemical, and medical analysis. Quantum sensors based on optically addressable spin defects in bulk semiconductors are typically employed for such purposes, but the 3D crystal structure of the sensor inhibits the sensitivity by limiting the proximity of the defects to the target spins. Here we demonstrate the detection of paramagnetic spins using spin defects hosted in hexagonal boron nitride (hBN), a van der Waals material which can be exfoliated into the 2D regime. We first create negatively charged boron vacancy (V_B^-) defects in a powder of ultrathin hBN nanoflakes ($<$ 10 atomic monolayers thick on average) and measure the longitudinal spin relaxation time (T_1) of this system. We then decorate the dry hBN nanopowder with paramagnetic Gd^{3+} ions and observe a clear T_1 quenching, under ambient conditions, consistent with the added magnetic noise. Finally, we demonstrate the possibility of performing spin measurements including T_1 relaxometry using solution-suspended hBN nanopowder. Our results highlight the potential and versatility of the hBN quantum sensor for a range of sensing applications, and make steps towards the realisation of a truly 2D, ultrasensitive quantum sensor.

Keywords: van der Waals, boron-vacancy, hexagonal boron nitride, magnetic noise, quantum sensing, spin relaxation

Optically addressable spin defects in solids have been a significant driver in the advancement of practical applications for highly sensitive quantum measurement and detection devices in a variety of fields including geoscience, materials science, and biology.[1–6] One promising capability of solid-state quantum sensors is being able to probe weak, fluctuating magnetic fields under ambient conditions and at sub-micrometer scales, which cannot typically be accessed by existing techniques such as nuclear magnetic resonance. The most prominent example of such a nanoscale sensor is the nitrogen-vacancy (NV) centre in diamond, which has been successfully employed to interrogate magnetic noise from a variety of sources, from magnons in ferromagnetic materials[7,8] to electric current fluctuations in conductors[9,10] to paramagnetic spins in molecular systems.[11–15] The detection of paramagnetic spins, *i.e.* unpaired electrons that produce a fast fluctuating magnetic noise, is especially relevant in the chemical, biological and medical sciences. For example, NV-based noise sensing has been applied to detect trace amounts of ions in aqueous solutions,[16,17] monitor the generation of free radicals in cells,[18,19] determine iron load in ferritin proteins,[20] and has been proposed as the basis for methods of rapid and sensitive virus detection.[21] In the latter proposal and similar biosensing demonstrations,[21,22] the biochemical signal of interest (*e.g.* the presence of a specific viral particle or a change of pH) is transduced into magnetic noise using a paramagnetic molecule, typically a gadolinium (Gd) complex, which is attached to the surface of the quantum sensor.

The method of choice in many of these applications is measuring the longitudinal spin relaxation time (T_1) of the defect, which is sensitive to magnetic fluctuations at the defect's spin resonance frequency, ω_0.[11–15] The change in relaxation rate induced by a nearby paramagnetic spin, $\Gamma_1^{\text{ext}} = 1/T_1^{\text{ext}}$, scales with the distance d between the sensor (spin defect) and the target spin as $\Gamma_1^{\text{ext}} \propto d^{-6}$.[11,12] The strong distance dependence suggests sensitivity to external spins is improved if defects are located nearer to the surface of the host crystal. However, spin defects in bulk 3D crystals face a practical limit, as the surface is typically plagued with dangling bonds and other sub-bandgap electronic states which compromise the charge- and photo-stability of near-surface defects.[23–25] For instance, an average minimum depth of at best or greater than $d \approx 5\,\text{nm}$ is typically observed for NV ensembles created near an optimised flat diamond surface,[26–28] despite individual NV centres being occasionally found at $d \approx 2\,\text{nm}$.[29] Additionally, these unwanted surface states are often paramagnetic[24,30] and cause a background magnetic noise obscuring the external signal of interest. These effects are especially severe in nanodiamonds with their high surface-to-volume ratio,[12] limiting their practical sensitivity to external signals. Given nanodiamonds are widely used for chemical and bio-sensing applications owing to their convenience and compatibility with in-solution measurements,[14,18,19,21,22,31] there is a strong motivation for exploring different quantum sensing systems which may afford shorter sensor-target distances and reduced intrinsic magnetic noise while preserving the versatility of nanodiamonds.

Spin defects hosted in a layered van der Waals (vdW) material could, in principle, provide a solution to both of these problems. Indeed, vdW materials can often be exfoliated into atomically thin flakes while maintaining near-perfect crystallinity and defect-free surfaces.[32] As such, it may be possible to engineer robust spin defects that reside within just a few atomic sites from the surface ($d \approx 1 - 2\,\mathrm{nm}$ corresponding *e.g.* to a trilayer flake with the defect in the middle layer) and with no surface-induced background magnetic noise, which could lead to future opportunities in ultrasensitive quantum sensing. Recently, hexagonal boron nitride (hBN) has emerged as a promising material platform to realise such ultrathin quantum sensors.[33–41] hBN is an exfoliable, air-stable vdW material and is host to a robust, optically addressable spin defect, the negatively charged boron vacancy (V_B^-).[33,42] The V_B^- defect can be introduced in the hBN lattice through a variety of irradiation methods,[43,44] and several demonstrations of quantum sensing have subsequently been reported, including the detection and imaging under ambient conditions of static magnetic fields, temperature and strain,[34,37–40] and the imaging of magnetic noise from a ferromagnetic material at cryogenic temperatures.[41]

In this work, we demonstrate the detection of magnetic noise from paramagnetic spins with an hBN quantum sensor, under ambient conditions. In contrast with previous quantum sensing demonstrations which employed hBN flakes exfoliated from bulk crystals,[34,37–40] here we use hBN nanopowder, an aggregate of nano-scale flakes, which forms a convenient, readily scalable, and cost-effective alternative for sensing in a wider range of environments including in solution. We first characterise the spin properties of the V_B^- defects created in hBN nanopowder, and find the T_1 time is comparable to that in a bulk hBN crystal. We then dress the nanopowder with Gd^{3+} ions, a common paramagnetic contrast agent used in magnetic resonance imaging, and observe a reliable T_1 quenching effect which illustrates the ability to detect external noise sources. Finally, we perform spin measurements of the nanopowder suspended in water and again observe a T_1 reduction upon adding Gd^{3+} ions, demonstrating the possibility of in-solution sensing experiments. These results establish hBN nanopowder as a promising platform for magnetic noise sensing applications, and motivate further work to improve the sensitivity of the hBN quantum sensor, including by making hBN flakes approaching the 2D limit. This could make hBN quantum sensors a viable alternative to nanodiamonds for a range of chemical and biosensing applications such as ultrasensitive virus detection and other rapid point-of-care tests.

Results and Discussion

Our quantum sensor is based on commercially available hBN nanopowder sourced from Graphene Supermarket. The powder is composed of flake-like particles with a thickness of 6 ± 3 nm (mean ± standard deviation) as determined by atomic force microscopy measurements, and a lateral size of order 100's nm (see methods and SI, Sec. I). The 6 nm mean thickness corresponds to ≈ 9 atomic monolayers. In principle, the size of these nanoflakes can be further reduced through liquid-phase exfoliation,[45–47] making it an ideal candidate to realise quantum sensors approaching the 2D limit (*i.e.* made up of a single monolayer of hBN). The as-received powder was electron irradiated to create a high density of vacancies throughout the entire material, some of which forming the desired $\mathrm{V_B^-}$ defects.[44] The irradiated powder was used as is, in its dry form, or suspended in water or isopropanol to make powder films by drop-casting or to perform in-solution measurements.

Spin measurements with hBN nanopowder

We first characterised the dry hBN nanopowder following electron irradiation, to establish a baseline of its optical and spin properties. To this end, the powder was placed directly onto the surface of a printed circuit board (PCB) with a microwave (MW) waveguide to enable driving of the $\mathrm{V_B^-}$'s electron spin transitions. A schematic of the experiment is shown in Fig. 1(a), and the crystal structure of the $\mathrm{V_B^-}$ defect in Fig. 1(b). Small clumps of hBN nanopowder are visible in the photograph Fig. 1(c), which were imaged using a widefield optical microscope [Fig. 1(d,e)]. The $\mathrm{V_B^-}$ defects are excited with a green laser ($\lambda = 532$ nm) and the resulting photoluminescence (PL) in the near-infrared ($\lambda = 750 - 900$ nm) imaged by a camera [Fig. 1(e)], showing uniform PL across the clump. The ground state of the $\mathrm{V_B^-}$ defect is a spin triplet ($S = 1$) which is polarised into the $|0\rangle$ state upon laser excitation

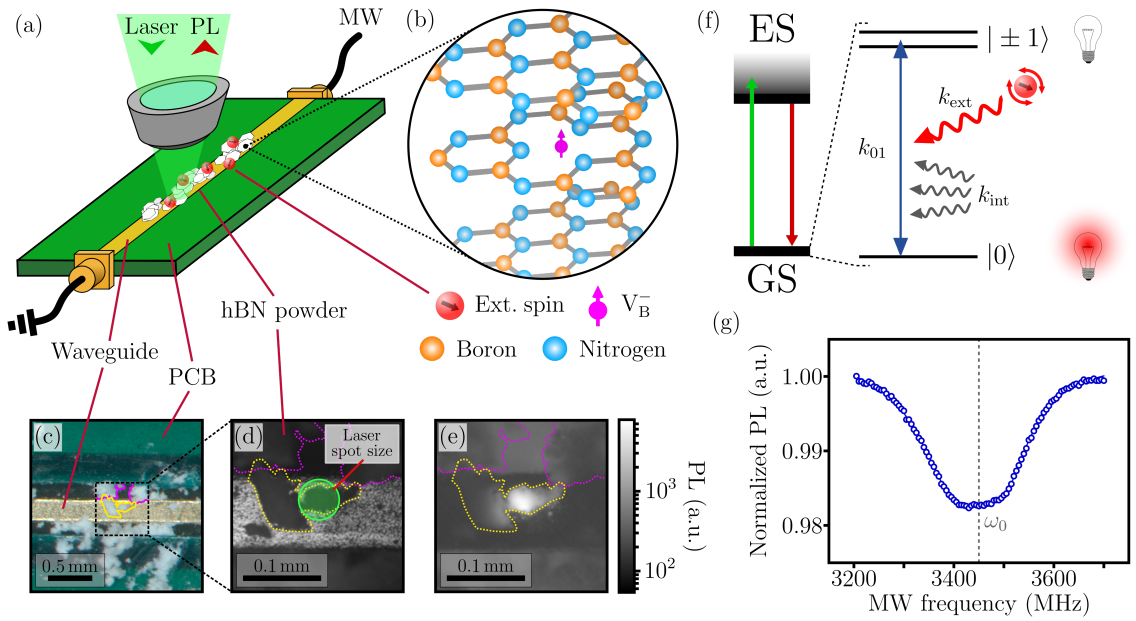

Figure 1: **Quantum sensing with hBN nanopowder**. (a) Schematic representation of the experimental setup. Electron-irradiated hBN nanopowder (represented as a collection of white flakes) is deposited onto a printed circuit board (PCB) with a microwave (MW) waveguide. The spin state of the V_B^- defects in the powder is optically measured via illumination with a green laser and collection of the photoluminescence (PL), which can be used to sense external paramagnetic spins (represented as red spheres) through their magnetic noise. (b) Crystal structure of the V_B^- defect in the hBN lattice. (c) True-colour photograph of hBN powder on the PCB. (d) Reflection micrograph (red channel only, displayed on a grey intensity scale) of a zoomed-in section from (c). Powder on the MW waveguide is outlined in yellow while on the PCB it is highlighted in pink. The approximate position and spot size of the laser used for PL measurements is also shown. (e) Corresponding PL image ($\lambda = 750-900\,\mathrm{nm}$ spectral band) taken under laser illumination ($\lambda = 532\,\mathrm{nm}$) and displayed on a log scale. (f) Simplified energy level structure of the V_B^- defect. Laser illumination populates the excited state (ES) which undergoes spin-dependent PL to return to the ground state (GS). This process selectively populates the GS spin sub-level $|0\rangle$. The population imbalance then decays back to equilibrium with a two-way transition rate $k_{01} = k_{\mathrm{int}} + k_{\mathrm{ext}}$ which has both intrinsic (k_{int}) and external (k_{ext}) contributions. The observed relaxation rate out of $|0\rangle$ is given by $\Gamma_1 = 3k_{01}$. (g) Typical pulsed-ODMR spectrum measured for the hBN nanopowder in zero magnetic field.

[Fig. 1(f)]. When left in the dark, this unequal population distribution decays back to thermal equilibrium (an equal mixture of all three spin states $|0, \pm 1\rangle$) at a rate $\Gamma_1 = 1/T_1$.[48] In general, the total relaxation rate is the sum of intrinsic and extrinsic contributions, $\Gamma_1 = \Gamma_1^{\mathrm{int}} + \Gamma_1^{\mathrm{ext}}$, where Γ_1^{ext} may be caused *e.g.* by paramagnetic spins external to the hBN crystal, as we will demonstrate later. Importantly, the spin state can be read out optically owing to spin-dependent PL,[33] which will allow Γ_1 to be measured. Moreover, by applying a MW field of variable frequency, an optically detected magnetic resonance (ODMR) spectrum can be obtained [Fig. 1(g)], revealing a broad resonance at $\omega_0 \approx 2\pi \times 3.45$ GHz corresponding to the electronic spin transitions $|0\rangle \rightarrow |\pm1\rangle$. The 2% spin contrast obtained in this pulsed-ODMR spectrum is in line with previous reports on similar powders.[36]

Intrinsic T_1 time

To assess the viability of the hBN nanopowder for T_1-based magnetic noise sensing, we first characterised the intrinsic T_1 time of the dry powder. The measurement sequence is depicted in Fig. 2(a) and consists of laser pulses, required to initialise and read out the spin state, separated by a dark time τ during which a T_1 decay takes place. A reference measurement including a resonant MW pulse is performed to remove common-mode variations and extract the spin imbalance, which decays towards zero as τ is increased, as shown in the example decay curves in Fig. 2(b). In principle all-optical measurements are also viable using an appropriate MW-free reference measurement.[49] Here, the PL data is integrated from a $15 \times 15\,\mu\text{m}^2$ region of powder which is uniformly illuminated by the laser. We found the curves are generally well fit by a mono-exponential function, $e^{-\tau/T_1}$, from which T_1 is obtained (see further analysis details in the SI, Sec. II).

In Fig. 2(b), two types of powder are measured and compared to a large ($\sim 100\,\mu$m) flake exfoliated from a high-purity bulk hBN crystal (PL image shown as inset of Fig. 2(b)). Powder 1 received the lowest electron irradiation dose ($2 \times 10^{18}\,\text{cm}^{-2}$) and returns $T_1 = 19.5 \pm 0.8\,\mu$s (here the uncertainty corresponds to the standard error from the fit). For powder 2, the irradiation dosage was increased by 2.5× to 5×10^{18} cm^{-2} and T_1 was measured as $T_1 = 17.6 \pm 0.6\,\mu$s. For the bulk crystal, which was electron irradiated to the same dose as powder 1, T_1 was slightly lower, $T_1 = 14.0 \pm 0.8\,\mu$s. The small differences in T_1 may be due to different levels of crystal damage, as was suggested by Guo et al.;[50] here we speculate that the powder may experience less damage than the bulk crystal at the same nominal irradiation

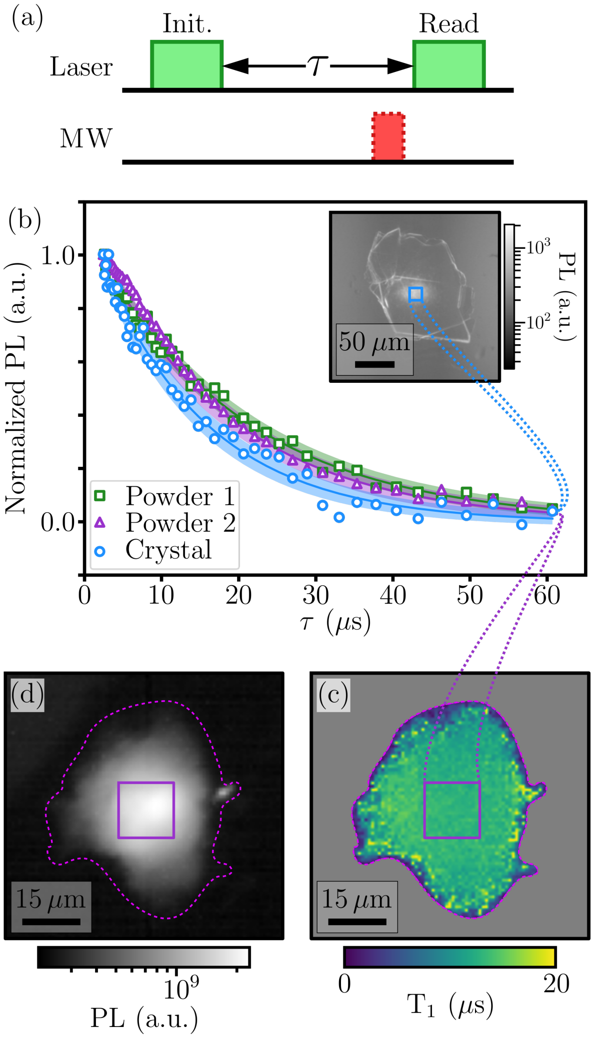

Figure 2: T_1 **relaxation in hBN nanopowder.** (a) Pulse sequence for T_1 measurements. The laser acts both to initialise the spin state and read it out through the PL intensity. For each dark time τ, two PL measurements are performed, with and without the MW pulse, for normalisation purposes. (b) Spin relaxation curves for the V_B^- defects in two nanopowder samples which received different irradiation doses (powder 2 higher than powder 1, see text) and in a bulk crystal flake. Solid lines are mono-exponential fit; shaded areas indicate one standard error for the fit parameters. Inset: PL image of the bulk crystal flake, displayed on a log scale. (c) Spatial map of T_1 for a clump of hBN nanopowder. Area external to the clump is masked as it contains no hBN powder. (d) The corresponding PL image of the clump plotted with a log scale.

dose due to more efficient thermalisation during the irradiation process. Importantly, the T_1 values measured for our nanopowders, despite a mean flake thickness of only 6 nm, are comparable to the value reported by Gottschol et al.[48] for a neutron-irradiated bulk crystal ($T_1 = 18\,\mu$s), which is the largest T_1 value reported to date for V_B^- at room temperature.

Thus, nanopowders appear as an ideal platform for T_1-based sensing, available in much higher volume and at a lower cost compared to flakes made from bulk crystals.

We also assessed possible T_1 spatial variations across a clump of hBN powder. A T_1 map is shown in Fig. 2(c) for a typical clump, with the corresponding PL image shown in Fig. 2(d). The measured T_1 is found to be relatively uniform across the clump, with a standard deviation of about $1\,\mu$s comparable with the uncertainty from the fitting of individual pixels. On a larger scale, we observed slightly larger variations up to ±10% for the mean T_1 of distinct clumps of powder of the same type, and from different spatial locations within a continuous film of powder (as we will see in Fig. 3). Such variations may be due to local temperature variations (as laser and MW absorption leads to some amount of heating) or reflect measurement and analysis uncertainties, see Sec. II and III of the SI for further discussions (including a derivation of the initialisation fidelity). In the following, we will study T_1 changes caused by external magnetic signals, keeping all measurement conditions constant otherwise.

Detection of external paramagnetic spins

We now test the possibility of detecting external paramagnetic spins with the hBN nanopowder, by adding a solution of gadolinium trichloride ($GdCl_3$). Due to the high spin of the Gd^{3+} ion ($S = \frac{7}{2}$), gadolinium complexes are commonly used as paramagnetic relaxation agents in magnetic resonance imaging. To allow for systematic measurements, we first prepare a uniform film of hBN nanopowder by suspending the powder [powder 2 from Fig. 2(b)] in isopropanol and drop-casting onto a MW waveguide [Fig. 3(a)]. A series of T_1 measurements are made at multiple random locations along the waveguide to gather a reference distribution of T_1 times, giving the top histogram in Fig. 3(b). The mean value is $T_1 = 16.3 \pm 1.3\,\mu$s where here the error bar corresponds to the standard deviation from the histogram. The spread is consistent with the variation of up to ±10% observed and discussed previously in relation to Fig. 2.

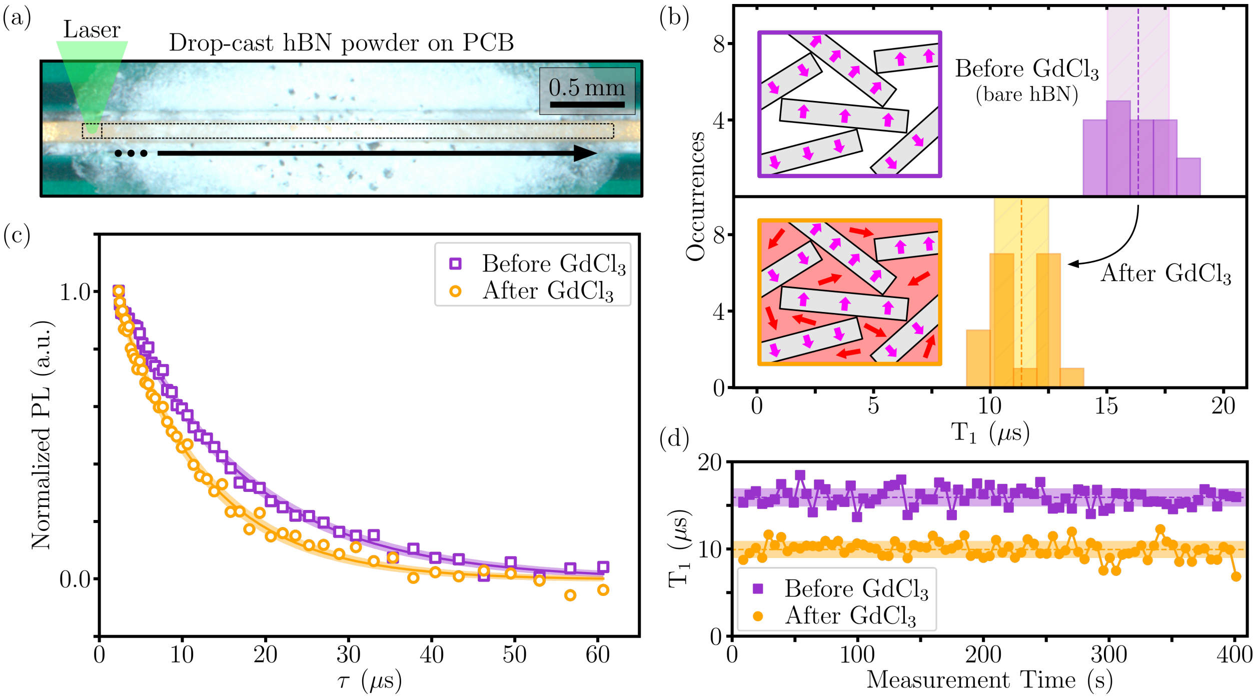

Figure 3: **Quenching T_1 with external paramagnetic spins**. (a) Photograph of hBN nanopowder film formed by drop-casting. Numerous T_1 measurements are taken at random distinct locations along the direction indicated by the arrow. The drop-cast nanopowder is then dosed with a solution of $GdCl_3$, and the T_1 measurements repeated. (b) Histograms for 20 T_1 measurements taken before (top histogram) and after (bottom) application of the $GdCl_3$ solution (100 mM concentration in water). The vertical dotted lines represent the average recorded T_1 and the shaded area is one standard deviation either side of the average. (c) Representative spin relaxation curves selected from each histogram in (b). Solid lines are mono-exponential fit; shaded areas indicate one standard error for the fit parameters. (d) Time traces of T_1 recorded before and after application of the $GdCl_3$ solution. Each data point corresponds to 5 s of signal integration.

Following these reference measurements, a drop of $GdCl_3$ solution is deposited on the hBN film and allowed to percolate through the powder. Evaporation of the water by heating then leaves the hBN nanoflakes surrounded by a highly concentrated medium of paramagnetic Gd^{3+} ions. Example relaxation curves before and after adding Gd^{3+} are plotted in Fig. 3(c), showing a clear T_1 reduction upon adding Gd^{3+}. Repeating the measurements at multiple locations [bottom histogram in Fig. 3(b)], we find that all T_1 values measured are shorter compared to the bare powder, with a mean value of $T_1 = 11.3 \pm 1.2\,\mu s$, a 30% reduction, significantly larger than the $\lesssim 10\%$ uncertainty. This T_1 reduction corresponds to an additional relaxation rate of $\Gamma_1^{\rm ext} = 30 \pm 10\,$kHz. Furthermore, we performed successive T_1 measurements (one every 5 s) at a given location and found T_1 to be stable over many minutes of monitoring [Fig. 3(d)], with again a clear offset in the presence of Gd^{3+}. Combined, these results indicate a robust T_1 quenching effect by the Gd^{3+} spins. Note, we repeated these experiments with higher concentrations of the GdCl$_3$ solution, and by applying multiple doses of the solution, and found a similar level of T_1 quenching in all cases, suggesting that the resulting density of Gd^{3+} spins around the hBN flakes has reached a saturation. On the other hand, repeating the process using pure water or a highly diluted GdCl$_3$ solution led to no measurable change in T_1.

To verify the observed T_1 reduction is consistent with magnetic noise from the Gd^{3+} spins, we assume each hBN nanoflake is surrounded by pure GdCl$_3$ and contain V_B^- defects located at a distance d from either surface of the flake of thickness $2d$ (see Sec. IV of the SI). The Gd^{3+} spins produce a randomly fluctuating magnetic field with a correlation time τ_c, which increases the relaxation rate of the V_B^- spins by[11,12]

$$\Gamma_1^{\rm ext} = 3\gamma_e^2 B_\perp^2 \frac{\tau_c}{1+\omega_0^2\tau_c^2}, \tag{1}$$

where γ_e is the electron gyromagnetic ratio and $B_\perp^2$ is the variance in the transverse magnetic field experienced by the V_B^- spins. $\Gamma_1^{\rm ext}$ is maximised when $\tau_c = 1/\omega_0 \approx 50\,$ps, which is a typical order of magnitude for Gd^{3+} complexes.[11] Assuming this maximum effect, we find the observed $\Gamma_1^{\rm ext}$ is reproduced for a flake thickness of $2d \approx 10\,$nm, in good agreement with the $6 \pm 3\,$nm thickness of our flakes. This supports our claim that the observed T_1 quenching is caused by the magnetic noise from the added Gd^{3+} spins.

Spin measurements in solution

Many applications of T_1-based sensing involve a liquid environment, for instance detecting ions and viruses in aqueous solutions[16,17,21] or free radicals in cells,[18,19] or to measure the pH

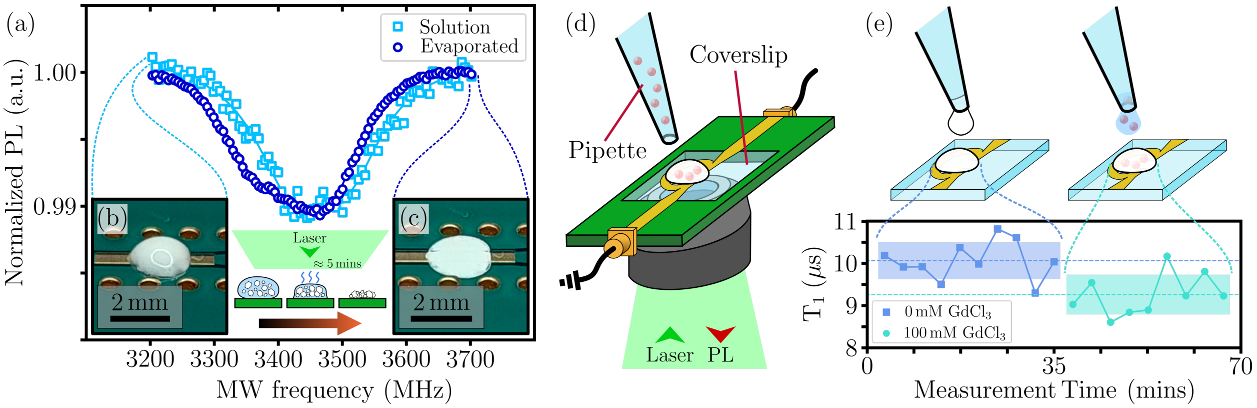

Figure 4: **Solution-based spin measurements**. (a) ODMR spectra from hBN nanopowder recorded before and after evaporation of the host water. (b,c) Photographs of the hBN nanopowder on the PCB before (b) and after (c) water evaporation. In (b), the powder forms a colloidal suspension, whereas in (c) the powder forms a dry film as in Fig. 3(a). (d) Schematic of the experimental setup for in-solution T_1 sensing. The inverted geometry facilitates addition of paramagnetic ions and minimises measurement-induced heating allowing extended measurement times. (e) Time trace of T_1 measured from the suspension, with 100 mM of GdCl$_3$ added after 35 minutes. The horizontal dashed lines represent the average T_1 from before and after adding GdCl$_3$, with the shading representing one standard deviation. Note, T_1 is shorter even in pure water compared to the dry powder, which may be due to a change in the internal spin or charge environment of the hBN flakes.

of a solution.[22] To test the sensing capabilities of hBN in a wet environment, we performed spin measurements of the nanopowder suspended in water. First, a drop of the hBN solution was placed on a MW waveguide and a pulsed-ODMR spectrum recorded [Fig. 4(a)]. As shown in the photographs Fig. 4(b), the solution has a white opaque appearance, such that the collected PL signal must initially come from the top-most part of the colloidal suspension. The water was found to evaporate completely after a few minutes of continuous measurement, leaving behind a dry hBN powder film [Fig. 4(c)]. Comparing the ODMR spectra taken before and after evaporation [Fig. 4(a)], we see that while the contrast remains relatively unchanged ($\approx 1\%$), the resonance is shifted towards lower frequencies by ≈ 50 MHz upon evaporation. This decrease in ω_0, which here corresponds to the zero-field splitting parameter of the V_B^- spin, implies an increase in local temperature of ≈ 70 K.[34,36] The rapid evaporation followed by a dramatic temperature increase can be explained by the presence of significant heating due to local laser and MW absorption, which is initially dissipated as latent heat during the evaporation phase thus keeping the solution relatively cool, until the water has fully evaporated.

To facilitate in-situ addition of paramagnetic spins to the solution and T_1 measurements over extended periods of time, we next moved to a setup based on an inverted microscope configuration [Fig. 4(d)]. The hBN suspension is deposited on a glass coverslip which comprises an Ω-shaped MW waveguide. Because optical addressing occurs from below, the collected PL signal comes primarily from the hBN flakes that are closest to the glass-solution interface, and so it is possible to address a region located very close to the MW waveguide, thus requiring a significantly reduced MW power. To further reduce the heating induced by the measurements, we used shorter laser pulses and a lower laser peak power. As a result, we were able to perform T_1 measurements continuously for up to an hour before complete evaporation of the water, although at the cost of a reduced signal-to-noise ratio – in future, a cuvette-based setup or microfluidic channels could be employed to allow optimised, long-term measurements.[51,52] As a test experiment, we monitored the T_1 time of the hBN flakes initially suspended in pure water, before adding a solution of 100 mM $GdCl_3$ [Fig. 4(e)]. A small reduction in T_1 is observed upon addition of the $GdCl_3$ solution, corresponding to an added relaxation rate of $\Gamma_1^{\mathrm{ext}} = 10 \pm 10\,\mathrm{kHz}$. While the observed T_1 change is close to the measurement uncertainty, these experiments demonstrate the feasibility of in-solution magnetic noise sensing with hBN nanopowder. Note, the induced quenching Γ_1^{ext} is smaller than that observed in Fig. 3, which is expected since here the density of Gd^{3+} ions is reduced due to the presence of solvent molecules. Using higher concentrations of Gd^{3+} ions led to additional background PL which made the T_1 measurements unreliable.

Sensitivity

The key motivation for developing quantum sensors based on vdW materials is the potential for a drastically reduced minimum distance d between sensor (spin defects) and target (*e.g.* paramagnetic spins), compared to 3D hosts like diamond. In the present work, for our initial demonstration of external paramagnetic spin detection, we used commercially available, off-the-shelf hBN nanopowders which had a flake thickness of $6 \pm 3\,\mathrm{nm}$, meaning the sensing defects are located at a typical depth of $3\,\mathrm{nm}$, which is already an improvement over state-of-the-art experiments based on NV ensembles in diamond.[26–28] Furthermore, there is ample room for optimisation of the hBN sensor, in particular liquid-phase exfoliation methods should provide a straightforward way to produce thinner hBN flakes in large quantities,[45–47] *e.g.* producing trilayer flakes with stable V_B^- defects in the middle layer is a plausible scenario. While there has been no report of V_B^- defects in trilayer hBN to date, V_B^- defects have been successfully detected in flakes as thin as 4 nm[53] while still exhibiting ODMR, implying the defects are within $2\,\mathrm{nm}$ (*i.e.* 3 atomic layers) of the closest surface. Compared to an NV centre at $d = 5$ nm (typical minimum depth observed[26–28]), a V_B^- defect at $d = 2$ nm would increase the relaxation rate Γ_1^ext induced by a paramagnetic spin located at the surface by a factor $(5/2)^6 = 244$, already a dramatic improvement. When detecting an ensemble of external paramagnetic spins as performed in this work, the scaling is $\Gamma_1^\mathrm{ext} \propto d^{-3}$ (see Sec. VI of the SI), which would lead to an increase in Γ_1^ext by $(3/1)^3 = 27$ in the hypothetical case of trilayer hBN flakes ($d \approx 1$ nm) compared with the presented hBN results (assuming $d \approx 3$ nm based on the mean thickness).

Nevertheless, a potential gain in Γ_1^ext due to better proximity does not guarantee an improved sensitivity to external spins. In a photon-shot-noise-limited T_1-relaxometry experiment, the signal-to-noise ratio scales as[11,12]

$$\mathrm{SNR} \propto \frac{\Gamma_1^\mathrm{ext}}{\sqrt{\Gamma_1^\mathrm{int}}}\mathcal{C}\sqrt{I_\mathrm{PL}}, \tag{2}$$

where $\Gamma_1^\mathrm{int} = 1/T_1^\mathrm{int}$ is the intrinsic relaxation rate in the absence of the target spin (assumed to satisfy $\Gamma_1^\mathrm{int} \gg \Gamma_1^\mathrm{ext}$), $\mathcal{C}$ is the relative spin contrast, and I_PL is the PL signal from one readout pulse. Currently, V_B^- defect ensembles exhibit inferior contrast and PL output compared to typical NV ensembles, and so will need to be improved through material optimisation (*e.g.*, to increase defect creation yield, as currently only a small fraction of boron vacancies are in the desired negatively charged state[54]) or photonics engineering to enhance collection.[35,53,55] On the other hand, the intrinsic relaxation time observed in this work for $\mathrm{V_B^-}$ in hBN nanopowders ($T_1^{\mathrm{int}} \approx 15 - 20\,\mu$s) is similar to that of NVs in nanodiamonds of comparable size of order 10 nm,[12] which do not reach the longer relaxation times exhibited by NVs in bulk diamond but nevertheless have found widespread interest. Considering all these factors together, we believe hBN nanopowders can be improved as a sensing platform to detect sub-millimolar concentrations of paramagnetic ions and emerge as a viable alternative to nanodiamonds for T_1 relaxometry in this concentration regime with the potential of a lower production cost, making it appealing for applications such as high-sensitivity point-of-care diagnostics.[21,31] Note, for these applications the development of robust surface functionalisation methods will be necessary.[56]

Conclusions

In this work, we demonstrated detection of magnetic noise from paramagnetic spins under ambient conditions using a van der Waals quantum sensor, namely using optically addressable spin defects ($\mathrm{V_B^-}$ defects) in hBN nanopowders. We first characterised the intrinsic spin relaxation time (T_1) of the $\mathrm{V_B^-}$ defects in nanopowders, which was found to be comparable to that in bulk hBN crystals. We then observed a reduction in T_1 upon the addition of paramagnetic $\mathrm{Gd^{3+}}$ ions, in dry conditions, demonstrating the ability to detect external noise sources. Finally, we performed spin measurements using the hBN nanopowder suspended in water, demonstrating the feasibility of in-solution sensing experiments. The sensitivity of the hBN quantum sensor for the detection of paramagnetic spins was discussed, and with major improvements (in particular, approaching the 2D limit for the host hBN flakes) could be competitive with established quantum sensing platforms such the NV centre in diamond. However, belying significant improvements to the performance of $\mathrm{V_B^-}$ as a quantum sensor, we establish opportunity to explore hBN as a host to other defects[57–59] which may be more promising candidates for sensing applications in 2D or near 2D structures. Our results thus suggest hBN nanopowders could be a viable and potentially more convenient and cost-effective alternative to diamond-based sensors, particularly in the micromolar to millimolar regime, making it appealing for a range of chemical and biosensing applications such as ultrasensitive virus detection and other rapid point-of-care tests.

Methods/Experimental

Experimental setup

The optical and spin measurements reported in the main text were carried out on a custom-built wide-field fluorescence microscope. Optical excitation from a continuous-wave (CW) $\lambda = 532$ nm laser (Laser Quantum Opus 2 W) was gated using an acousto-optic modulator (Gooch & Housego R35085-5) and focused using a widefield lens ($f = 400$ mm) to the back apearture of the objective lens (Nikon S Plan Fluor ELWD 20x, NA = 0.45). The photoluminescence (PL) from the V_B^- defects is separated from the excitation light with a dichroic mirror and filtered using a 750 nm longpass filter before being imaged using a tube lens ($f = 300$ mm) onto a scientific CMOS camera (Andor Zyla 5.5-W USB3). In all experiments except Fig. 4(d,e) of the main text, the laser spot diameter ($1/e^2$) at the sample was about $50\,\mu$m and the total CW laser power 500 mW, which gives a maximum intensity of about $0.5\,\mathrm{mW}/\mu\mathrm{m}^2$ in the centre of the spot. In Fig. 4(d,e), the laser power was reduced to 200 mW. In principle, the laser power can be further reduced at a loss of sensitivity.

Microwave (MW) excitation was provided by a signal generator (Windfreak SynthNV PRO) gated using an IQ modulator (Texas Instruments TRF37T05EVM) and amplified (Mini-Circuits HPA-50W-63+). A pulse pattern generator (SpinCore PulseBlasterESR-PRO 500 MHz) was used to gate the excitation laser and MW and to synchronise the image acquisition. The output of the amplifier was connected to the printed circuit board (PCB) which was terminated by a 50 Ω termination. In all experiments except Fig. 4(d,e), MW driving was achieved via a coplanar waveguide built in the PCB, with the hBN powder deposited directly onto the surface of the waveguide. In Fig. 4(d,e), the MW was delivered by an Ω-shaped resonator fabricated onto a glass coverslip mounted on a PCB, with the hBN suspension deposited on the coverslip. All measurements were performed at room temperature in ambient atmosphere.

Sample preparation

All experiments performed in this work [except the bulk crystal measurement in Fig. 2(b)] used hBN nanopowder sourced from Graphene Supermarket (BN Ultrafine Powder). As the as-received powder contained no measurable concentration of V_B^- defects, we subjected the powder to electron irradiation with a beam energy of 2 MeV. The irradiation dose was $2 \times 10^{18}\,\mathrm{cm}^{-2}$ (called 'powder 1') or $5 \times 10^{18}\,\mathrm{cm}^{-2}$ ('powder 2'). PL spectra of the different powders under $\lambda = 532\,\mathrm{nm}$ excitation show the appearance of the characteristic V_B^- emission upon irradiation *i.e.* a broad peak centred around 800 nm wavelength[33] (see Supporting Information Fig. S1 for details). Spectra were obtained with the same experimental setup described above, with 500 mW of laser power over a 50 μm spot, except that the PL emission was passed through a 550 nm longpass filter to block the laser light and sent to a spectrometer (Ocean Insight Maya2000-Pro).

For the experiments in Fig. 1 and 2, the irradiated powder was transferred to the PCB with the tip of a pair of tweezers, forming large clumps (10's of μm in size). For the experiments in Fig. 3, the irradiated powder was suspended in isopropyl alcohol (IPA) at a concentration of 20 mg/mL and sonicated for 30 min using a horn-sonicator. The sediment from the suspension was drawn using a pipette, then drop cast on the PCB, forming a relatively continuous film. For the experiments in Fig. 4, the powder was suspended in water (20 mg/mL) and a drop of the suspension was deposited on the PCB [Fig. 4(a-c)] or on the coverslip [Fig. 4(d,e)].

To characterise the size of the hBN nanoflakes, we performed atomic force microscope (AFM) measurements of powder 2. The particle stock suspension (20 mg/mL in IPA) was diluted to a concentration of 1 mg/mL, sonicated for 10 min in a sonication bath, centrifuged at 1000 rcf for 1 min to remove large aggregates, and the supernatant was spin coated at 2000 rpm onto a clean silicon wafer. AFM images were acquired using an Oxford Instruments Asylum Research MFP-3D Infinity AFM in AC mode using a Budget Sensors Tap300AL-G probe. The images were collected at a scan rate of 1 Hz. Typical AFM images and height profiles are shown in the Supporting Information, Fig. S2(a-e). The images were analysed to extract the average thickness of each individual flake, excluding all large particle aggregates and plotted in a histogram (see Supporting Information, Fig. S2(f)). The average flake thickness ranges mainly between 2 nm and 9 nm, with a mean value of 6 nm and a standard deviation of 3 nm. The lateral size of the flakes is of the order of 100's nm. These values are consistent with previous measurements of powder from the same manufacturer.[47] They are also consistent with the specific surface area of $\sim 20\,\mathrm{m}^2/\mathrm{g}$ measured by the manufacturer.

For the T_1 quenching experiments reported in Fig. 3 and 4, a solution of $\mathrm{GdCl_3}$ was first prepared by dissolving $\mathrm{GdCl_3}$ solid powder (Sigma-Aldrich, 99.99% purity) in water to a concentration of 100 mM. A drop of the solution was then deposited on the hBN film. The PCB was then heated immediately to 80°C for 5 min to evaporate any remaining water. We note that the density of the hBN nanopowder in dry form is $0.30\,\mathrm{g/cm}^3$ according to the manufacturer, which is 7 times less than the density of bulk hBN ($2.1\,\mathrm{g/cm}^3$). This indicates that the dry powder forms a largely porous medium. We conjecture that the $\mathrm{GdCl_3}$ solution percolates through the hBN film in such a way that most individual hBN flakes are completely surrounded by $\mathrm{GdCl_3}$ upon solvent evaporation, as depicted in the inset of Fig. 3(b).

Finally, the bulk crystal measurement in Fig. 2(b) was done using a high-purity crystal purchased from HQ Graphene. The crystal was electron irradiated to a dose of $2 \times 10^{18}\,\mathrm{cm}^{-2}$ with a beam energy of 2 MeV. Following irradiation, a $\sim 1\,\mu$m-thick flake was exfoliated using scotch tape and transferred to a quartz coverslip placed on a PCB with a MW waveguide.

To avoid possible edge effects, the T_1 time was measured near the centre of the flake where the PL from the V_B^- defects was uniform.

Data acquisition

The spin measurements reported in the paper were obtained using the prior described wide-field setup. For optically detected magnetic resonance (ODMR) spectra, the pulse sequence was typically: $0.5\,\mu$s laser pulse, $0.5\,\mu$s wait time, 30 ns MW pulse (corresponding to a π spin flip as estimated from a Rabi measurement). This sequence was repeated thousands of times to fill the exposure time of the camera, generally set to 10 ms. The MW frequency was swept such that one camera frame is recorded for each MW frequency value, with a reference frame with the MW off recorded every other frame to remove common-mode noise – forming a normalised ODMR spectrum (PL with MW on divided by PL with MW off) such as that shown in Fig. 1(g). The MW sweep was repeated tens to hundreds of times to improve the signal-to-noise ratio (SNR), corresponding to several minutes of acquisition per spectrum.

T_1 measurements were obtained by applying a series of laser pulses separated by a variable dark time τ. For each τ value, the base pulse sequence (laser pulse, wait time τ, optional MW pulse) was repeated $N = t_{\text{cam}}/t_0$ times where t_0 is the duration of the base sequence with the shortest τ, and $t_{\text{cam}} = 10\,\text{ms}$ is the minimum camera exposure time. As τ is increased, we keep N fixed and increase the camera exposure time accordingly. For each τ value, a camera frame is acquired without the MW pulse ('signal'), followed by a camera frame with the MW pulse ('reference'). Example PL traces $S(\tau)$ and $R(\tau)$ thus obtained (without and with the MW pulse, respectively), are shown in the Supporting Information, Fig. S3. The reference trace serves to remove common-mode variations and normalise the data, discussed further in the supporting information. The entire τ sweep is repeated over several minutes to improve the SNR in the same way we do for ODMR measurements.

The laser pulse acts as both initialisation and readout of the V_B^- spin state. Its duration (between $0.5\,\mu$s and $4\,\mu$s in our experiments) is chosen long enough to initialise the spin in the

$|0\rangle$ state with sufficient fidelity as appropriate for T_1 measurements while preserving a good spin contrast, see supporting information. The MW pulse was around 30 ns long typically, corresponding to a π spin flip as estimated from a Rabi measurement. The dark time τ was defined as the time between consecutive laser pulses, inclusive of the MW pulse time when present. The timing of the MW pulse was adjusted to account for the delay incurred by the AOM, such that the MW pulse occurred immediately prior to the laser pulse. For all T_1 measurements presented in the paper, 51 τ points are collected between $2\,\mu$s to $60\,\mu$s with exponentially weighted spacing, where we excluded the $\tau = 0 - 2\,\mu$s range to allow the system to fully relax to its electronic ground state.

Except in Fig. 2(c) where the T_1 data was analysed pixel by pixel to form a spatial map of T_1, all ODMR and T_1 measurements reported integrated the data over a $15 \times 15\,\mu\text{m}^2$ area where the laser intensity was approximately uniform.

Acknowledgements

This work was supported by the Australian Research Council (ARC) through grants CE170100012, CE200100010, FT200100073, DE200100279 and FT220100053, and by the Office of Naval Research Global (N62909-22-1-2028). We thank Yongliang Chen for providing AFM data. The work was performed in part at the RMIT Micro Nano Research Facility (MNRF) in the Victorian Node of the Australian National Fabrication Facility (ANFF) and the RMIT Microscopy and Microanalysis Facility (RMMF). I.O.R. and A.J.H. are supported by an Australian Government Research Training Program Scholarship. S.C.S gratefully acknowledges the support of an Ernst and Grace Matthaei scholarship. P.R. acknowledges support through an RMIT University Vice-Chancellor's Research Fellowship. Part of this study was supported by QST President's Strategic Grant "QST International Research Initiative".

Supporting Information

The Supporting Information contains additional sample characterisation data, a detailed description of our T_1 data analysis methods, additional temperature-dependent T_1 data, and the details of the magnetic noise modelling.

References

1. Degen, C. L.; Reinhard, F.; Cappellaro, P. Quantum sensing. *Reviews of Modern Physics* **2017**, *89*, 035002.
2. Schirhagl, R.; Chang, K.; Loretz, M.; Degen, C. L. Nitrogen-Vacancy Centers in Diamond: Nanoscale Sensors for Physics and Biology. *Annual Review of Physical Chemistry* **2014**, *65*, 83–105.
3. Rondin, L.; Tetienne, J.-P.; Hingant, T.; Roch, J.-F.; Maletinsky, P.; Jacques, V. Magnetometry with nitrogen-vacancy defects in diamond. *Reports on Progress in Physics* **2014**, *77*, 056503.
4. Casola, F.; van der Sar, T.; Yacoby, A. Probing condensed matter physics with magnetometry based on nitrogen-vacancy centres in diamond. *Nature Reviews Materials* **2018**, *3*, 17088.
5. Wolfowicz, G.; Heremans, F. J.; Anderson, C. P.; Kanai, S.; Seo, H.; Gali, A.; Galli, G.; Awschalom, D. D. Quantum guidelines for solid-state spin defects. *Nature Reviews Materials* **2021**, *6*, 906–925.
6. Aharonovich, I.; Tetienne, J.-P.; Toth, M. Quantum Emitters in Hexagonal Boron Nitride. *Nano Letters* **2022**, *22*, 9227–9235.
7. Du, C.; van der Sar, T.; Zhou, T. X.; Upadhyaya, P.; Casola, F.; Zhang, H.; Onbasli, M. C.; Ross, C. A.; Walsworth, R. L.; Tserkovnyak, Y.; Yacoby, A. Control and

local measurement of the spin chemical potential in a magnetic insulator. *Science* **2017**, *357*, 195–198.

8. McCullian, B. A.; Thabt, A. M.; Gray, B. A.; Melendez, A. L.; Wolf, M. S.; Safonov, V. L.; Pelekhov, D. V.; Bhallamudi, V. P.; Page, M. R.; Hammel, P. C. Broadband multi-magnon relaxometry using a quantum spin sensor for high frequency ferromagnetic dynamics sensing. *Nat Communications* **2020**, *11*, 5229.

9. Kolkowitz, S.; Safira, A.; High, A. A.; Devlin, R. C.; Choi, S.; Unterreithmeier, Q. P.; Patterson, D.; Zibrov, A. S.; Manucharyan, V. E.; Park, H.; Lukin, M. D. Probing Johnson noise and ballistic transport in normal metals with a single-spin qubit. *Science* **2015**, *347*, 1129–1132.

10. Ariyaratne, A.; Bluvstein, D.; Myers, B. A.; Jayich, A. C. B. Nanoscale electrical conductivity imaging using a nitrogen-vacancy center in diamond. *Nature Communications* **2018**, *9*, 2406.

11. Steinert, S.; Ziem, F.; Hall, L. T.; Zappe, A.; Schweikert, M.; Götz, N.; Aird, A.; Balasubramanian, G.; Hollenberg, L.; Wrachtrup, J. Magnetic spin imaging under ambient conditions with sub-cellular resolution. *Nature Communications* **2013**, *4*, 1607.

12. Tetienne, J.-P.; Hingant, T.; Rondin, L.; Cavaillès, A.; Mayer, L.; Dantelle, G.; Gacoin, T.; Wrachtrup, J.; Roch, J.-F.; Jacques, V. Spin relaxometry of single nitrogen-vacancy defects in diamond nanocrystals for magnetic noise sensing. *Physical Review B* **2013**, *87*, 235436.

13. Ermakova, A.; Pramanik, G.; Cai, J. M.; Algara-Siller, G.; Kaiser, U.; Weil, T.; Tzeng, Y. K.; Chang, H. C.; McGuinness, L. P.; Plenio, M. B.; Naydenov, B.; Jelezko, F. Detection of a few metallo-protein molecules using color centers in nanodiamonds. *Nano Letters* **2013**, *13*, 3305–3309.

14. Kaufmanna, S.; Simpson, D. A.; Hall, L. T.; Perunicic, V.; Senn, P.; Steinert, S.; McGuinness, L. P.; Johnson, B. C.; Ohshima, T.; Caruso, F.; Wrachtrup, J.; Scholten, R. E.; Mulvaney, P.; Hollenberg, L. Detection of atomic spin labels in a lipid bilayer using a single-spin nanodiamond probe. *Proceedings of the National Academy of Sciences of the United States of America* **2013**, *110*, 10894–10898.

15. Sushkov, A. O.; Chisholm, N.; Lovchinsky, I.; Kubo, M.; Lo, P. K.; Bennett, S. D.; Hunger, D.; Akimov, A.; Walsworth, R. L.; Park, H.; Lukin, M. D. All-optical sensing of a single-molecule electron spin. *Nano Letters* **2014**, *14*, 6443–8.

16. Ziem, F. C.; Götz, N. S.; Zappe, A.; Steinert, S.; Wrachtrup, J. Highly Sensitive Detection of Physiological Spins in a Microfluidic Device. *Nano Letters* **2013**, *13*, 4093–4098.

17. Simpson, D. A.; Ryan, R. G.; Hall, L. T.; Panchenko, E.; Drew, S. C.; Petrou, S.; Donnelly, P. S.; Mulvaney, P.; Hollenberg, L. C. L. Electron paramagnetic resonance microscopy using spins in diamond under ambient conditions. *Nature Communications* **2017**, *8*, 458.

18. Sharmin, R.; Nusantara, A. C.; Nie, L.; Wu, K.; Elias Llumbet, A.; Woudstra, W.; Mzyk, A.; Schirhagl, R. Intracellular Quantum Sensing of Free-Radical Generation Induced by Acetaminophen (APAP) in the Cytosol, in Mitochondria and the Nucleus of Macrophages. *ACS Sensors* **2022**, *7*, 3326–3334.

19. Nie, L.; Nusantara, A. C.; Damle, V. G.; Baranov, M. V.; Chipaux, M.; Reyes-San-Martin, C.; Hamoh, T.; Epperla, C. P.; Guricova, M.; Cigler, P.; van den Bogaart, G.; Schirhagl, R. Quantum Sensing of Free Radicals in Primary Human Dendritic Cells. *Nano Letters* **2022**, *22*, 1818–1825.

20. Grant, E. S.; Hall, L. T.; Hollenberg, L. C. L.; McColl, G.; Simpson, D. A. Nonmonotonic Superparamagnetic Behavior of the Ferritin Iron Core Revealed via Quantum Spin Relaxometry. *ACS Nano* **2023**, *17*, 372–381.

21. Li, C.; Soleyman, R.; Kohandel, M.; Cappellaro, P. SARS-CoV-2 Quantum Sensor Based on Nitrogen-Vacancy Centers in Diamond. *Nano Letters* **2022**, *22*, 43–49.

22. Rendler, T.; Neburkova, J.; Zemek, O.; Kotek, J.; Zappe, A.; Chu, Z.; Cigler, P.; Wrachtrup, J. Optical imaging of localized chemical events using programmable diamond quantum nanosensors. *Nature Communications* **2017**, *8*, 14701.

23. Kaviani, M.; Deak, P.; Aradi, B.; Frauenheim, T.; Chou, J. P.; Gali, A. Proper surface termination for luminescent near-surface NV centers in diamond. *Nano Letters* **2014**, *14*, 4772–7.

24. Stacey, A.; Dontschuk, N.; Chou, J.; Broadway, D. A.; Schenk, A. K.; Sear, M. J.; Tetienne, J.; Hoffman, A.; Prawer, S.; Pakes, C. I.; Tadich, A.; de Leon, N. P.; Gali, A.; Hollenberg, L. C. L. Evidence for Primal sp2 Defects at the Diamond Surface: Candidates for Electron Trapping and Noise Sources. *Advanced Materials Interfaces* **2018**, *6*, 1801449.

25. Bluvstein, D.; Zhang, Z.; Jayich, A. C. B. Identifying and Mitigating Charge Instabilities in Shallow Diamond Nitrogen-Vacancy Centers. *Phys Rev Lett* **2019**, *122*, 076101.

26. Ziem, F.; Garsi, M.; Fedder, H.; Wrachtrup, J. Quantitative nanoscale MRI with a wide field of view. *Scientific Reports* **2019**, *9*, 12166.

27. Healey, A. J.; Hall, L. T.; White, G. A.; Teraji, T.; Sani, M. A.; Separovic, F.; Tetienne, J. P.; Hollenberg, L. C. Polarization Transfer to External Nuclear Spins Using Ensembles of Nitrogen-Vacancy Centers. *Physical Review Applied* **2021**, *15*, 054052.

28. Liu, K. S.; Henning, A.; Heindl, M. W.; Allert, R. D.; Bartl, J. D.; Sharp, I. D.; Rizzato, R.; Bucher, D. B. Surface NMR using quantum sensors in diamond. *Proc. Natl. Acad. Sci. U.S.A.* **2022**, *119*, e2111607119.

29. Loretz, M.; Pezzagna, S.; Meijer, J.; Degen, C. L. Nanoscale nuclear magnetic resonance with a 1.9-nm-deep nitrogen-vacancy sensor. *Applied Physics Letters* **2014**, *104*, 033102.

30. Sangtawesin, S.; Dwyer, B. L.; Srinivasan, S.; Allred, J. J.; Rodgers, L. V. H.; De Greve, K.; Stacey, A.; Dontschuk, N.; O'Donnell, K. M.; Hu, D.; Evans, D. A.; Jaye, C.; Fischer, D. A.; Markham, M. L.; Twitchen, D. J.; Park, H.; Lukin, M. D.; de Leon, N. P. Origins of Diamond Surface Noise Probed by Correlating Single-Spin Measurements with Surface Spectroscopy. *Phys. Rev. X* **2019**, *9*, 031052.

31. Miller, B. S.; Bezinge, L.; Gliddon, H. D.; Huang, D.; Dold, G.; Gray, E. R.; Heaney, J.; Dobson, P. J.; Nastouli, E.; Morton, J. J. L.; McKendry, R. A. Spin-enhanced nanodiamond biosensing for ultrasensitive diagnostics. *Nature* **2020**, *587*, 588–593.

32. Novoselov, K. S.; Geim, A. K.; Morozov, S. V.; Jiang, D.; Zhang, Y.; Dubonos, S. V.; Grigorieva, I. V.; Firsov, A. A. Electric Field Effect in Atomically Thin Carbon Films. *Science* **2004**, *306*, 666–669.

33. Gottscholl, A.; Kianinia, M.; Soltamov, V.; Orlinskii, S.; Mamin, G.; Bradac, C.; Kasper, C.; Krambrock, K.; Sperlich, A.; Toth, M.; Aharonovich, I.; Dyakonov, V. Initialization and read-out of intrinsic spin defects in a van der Waals crystal at room temperature. *Nature Materials* **2020**, *19*, 540–545.

34. Gottscholl, A.; Diez, M.; Soltamov, V.; Kasper, C.; Krausse, D.; Sperlich, A.; Kianinia, M.; Bradac, C.; Aharonovich, I.; Dyakonov, V. Spin defects in hBN as promising temperature, pressure and magnetic field quantum sensors. *Nature Communications* **2021**, *12*, 4480.

35. Gao, X.; Jiang, B.; Llacsahuanga Allcca, A. E.; Shen, K.; Sadi, M. A.; Solanki, A. B.; Ju, P.; Xu, Z.; Upadhyaya, P.; Chen, Y. P.; Bhave, S. A.; Li, T. High-Contrast Plasmonic-Enhanced Shallow Spin Defects in Hexagonal Boron Nitride for Quantum Sensing. *Nano Letters* **2021**, *21*, 7708–7714.

36. Liu, W.; Li, Z.-P.; Yang, Y.-Z.; Yu, S.; Meng, Y.; Wang, Z.-A.; Li, Z.-C.; Guo, N.-J.; Yan, F.-F.; Li, Q.; Wang, J.-F.; Xu, J.-S.; Wang, Y.-T.; Tang, J.-S.; Li, C.-F.; Guo, G.-C. Temperature-Dependent Energy-Level Shifts of Spin Defects in Hexagonal Boron Nitride. *ACS Photonics* **2021**, *8*, 1889–1895.

37. Healey, A. J.; Scholten, S. C.; Yang, T.; Scott, J. A.; Abrahams, G. J.; Robertson, I. O.; Hou, X. F.; Guo, Y. F.; Rahman, S.; Lu, Y.; Kianinia, M.; Aharonovich, I.; Tetienne, J.-P. Quantum microscopy with van der Waals heterostructures. *Nature Physics* **2023**, *19*, 87–91.

38. Kumar, P.; Fabre, F.; Durand, A.; Clua-Provost, T.; Li, J.; Edgar, J.; Rougemaille, N.; Coraux, J.; Marie, X.; Renucci, P.; Robert, C.; Robert-Philip, I.; Gil, B.; Cassabois, G.; Finco, A.; Jacques, V. Magnetic Imaging with Spin Defects in Hexagonal Boron Nitride. *Phys. Rev. Appl.* **2022**, *18*, L061002.

39. Lyu, X.; Tan, Q.; Wu, L.; Zhang, C.; Zhang, Z.; Mu, Z.; Zúñiga-Pérez, J.; Cai, H.; Gao, W. Strain Quantum Sensing with Spin Defects in Hexagonal Boron Nitride. *Nano Letters* **2022**, *22*, 6553–6559.

40. Yang, T.; Mendelson, N.; Li, C.; Gottscholl, A.; Scott, J.; Kianinia, M.; Dyakonov, V.; Toth, M.; Aharonovich, I. Spin defects in hexagonal boron nitride for strain sensing on nanopillar arrays. *Nanoscale* **2022**, *14*, 5239–5244.

41. Huang, M.; Zhou, J.; Chen, D.; Lu, H.; McLaughlin, N. J.; Li, S.; Alghamdi, M.; Djugba, D.; Shi, J.; Wang, H.; Du, C. R. Wide field imaging of van der Waals ferromagnet Fe3GeTe2 by spin defects in hexagonal boron nitride. *Nature Communications* **2022**, *13*, 5369.

42. Liu, W.; Guo, N.-J.; Yu, S.; Meng, Y.; Li, Z.-P.; Yang, Y.-Z.; Wang, Z.-A.; Zeng, X.-D.; Xie, L.-K.; Li, Q.; Wang, J.-F.; Xu, J.-S.; Wang, Y.-T.; Tang, J.-S.; Li, C.-F.; Guo, G.-C.

Spin-active defects in hexagonal boron nitride. *Materials for Quantum Technology* **2022**, *2*, 032002.

43. Kianinia, M.; White, S.; Fröch, J. E.; Bradac, C.; Aharonovich, I. Generation of Spin Defects in Hexagonal Boron Nitride. *ACS Photonics* **2020**, *7*, 2147–2152.
44. Murzakhanov, F. F.; Yavkin, B. V.; Mamin, G. V.; Orlinskii, S. B.; Mumdzhi, I. E.; Gracheva, I. N.; Gabbasov, B. F.; Smirnov, A. N.; Davydov, V. Y.; Soltamov, V. A. Creation of Negatively Charged Boron Vacancies in Hexagonal Boron Nitride Crystal by Electron Irradiation and Mechanism of Inhomogeneous Broadening of Boron Vacancy-Related Spin Resonance Lines. *Nanomaterials (Basel)* **2021**, *11*, 1373.
45. Shen, J.; He, Y.; Wu, J.; Gao, C.; Keyshar, K.; Zhang, X.; Yang, Y.; Ye, M.; Vajtai, R.; Lou, J.; Ajayan, P. M. Liquid Phase Exfoliation of Two-Dimensional Materials by Directly Probing and Matching Surface Tension Components. *Nano Letters* **2015**, *15*, 5449–5454.
46. Zhang, K.; Feng, Y.; Wang, F.; Yang, Z.; Wang, J. Two dimensional hexagonal boron nitride (2D-hBN): synthesis, properties and applications. *J. Mater. Chem. C* **2017**, *5*, 11992–12022.
47. Chen, Y.; Westerhausen, M. T.; Li, C.; White, S.; Bradac, C.; Bendavid, A.; Toth, M.; Aharonovich, I.; Tran, T. T. Solvent-Exfoliated Hexagonal Boron Nitride Nanoflakes for Quantum Emitters. *ACS Applied Nano Materials* **2021**, *4*, 10449–10457.
48. Gottscholl, A.; Diez, M.; Soltamov, V.; Kasper, C.; Sperlich, A.; Kianinia, M.; Bradac, C.; Aharonovich, I.; Dyakonov, V. Room temperature coherent control of spin defects in hexagonal boron nitride. *Science Advances* **2021**, *7*, eabf3630.
49. Wood, J. D. A.; Broadway, D. A.; Hall, L. T.; Stacey, A.; Simpson, D. A.; Tetienne, J.-P.; Hollenberg, L. C. L. Wide-band nanoscale magnetic resonance spectroscopy using quantum relaxation of a single spin in diamond. *Physical Review B* **2016**, *94*, 155402.

50. Guo, N.-J.; Liu, W.; Li, Z.-P.; Yang, Y.-Z.; Yu, S.; Meng, Y.; Wang, Z.-A.; Zeng, X.-D.; Yan, F.-F.; Li, Q.; Wang, J.-F.; Xu, J.-S.; Wang, Y.-T.; Tang, J.-S.; Li, C.-F.; Guo, G.-C. Generation of Spin Defects by Ion Implantation in Hexagonal Boron Nitride. *ACS Omega* **2022**, *7*, 1733–1739.

51. Grant, E. S.; Olia, M. B. A.; Walsh, E. P.; Hall, L. T.; McColl, G.; Simpson, D. A. Method for in-solution, high-throughput T1 relaxometry using fluorescent nanodiamonds. 2022, 2211.14959. arXiv. https://doi.org/10.48550/arXiv.2211.14959 (accessed June 27, 2023).

52. Smits, J.; Damron, J. T.; Kehayias, P.; McDowell, A. F.; Mosavian, N.; Fescenko, I.; Ristoff, N.; Laraoui, A.; Jarmola, A.; Acosta, V. M. Two-dimensional nuclear magnetic resonance spectroscopy with a microfluidic diamond quantum sensor. *Science Advances* **2019**, *5*, eaaw7895.

53. Xu, X.; Solanki, A. B.; Sychev, D.; Gao, X.; Peana, S.; Baburin, A. S.; Pagadala, K.; Martin, Z. O.; Chowdhury, S. N.; Chen, Y. P.; Taniguchi, T.; Watanabe, K.; Rodionov, I. A.; Kildishev, A. V.; Li, T.; Upadhyaya, P.; Boltasseva, A.; Shalaev, V. M. Greatly Enhanced Emission from Spin Defects in Hexagonal Boron Nitride Enabled by a Low-Loss Plasmonic Nanocavity. *Nano Letters* **2023**, *23*, 25–33.

54. Gong, R.; He, G.; Gao, X.; Ju, P.; Liu, Z.; Ye, B.; Henriksen, E. A.; Li, T.; Zu, C. Coherent dynamics of strongly interacting electronic spin defects in hexagonal boron nitride. *Nature Communications* **2023**, *14*, 3299.

55. Froch, J. E.; Spencer, L. P.; Kianinia, M.; Totonjian, D. D.; Nguyen, M.; Gottscholl, A.; Dyakonov, V.; Toth, M.; Kim, S.; Aharonovich, I. Coupling Spin Defects in Hexagonal Boron Nitride to Monolithic Bullseye Cavities. *Nano Letters* **2021**, *21*, 6549–6555.

56. Weng, Q.; Wang, X.; Wang, X.; Bando, Y.; Golberg, D. Functionalized hexagonal boron

nitride nanomaterials: emerging properties and applications. *Chemical Society Reviews* **2016**, *45*, 3989–4012.

57. Mendelson, N.; Chugh, D.; Reimers, J. R.; Cheng, T. S.; Gottscholl, A.; Long, H.; Mellor, C. J.; Zettl, A.; Dyakonov, V.; Beton, P. H.; Novikov, S. V.; Jagadish, C.; Tan, H. H.; Ford, M. J.; Toth, M.; Bradac, C.; Aharonovich, I. Identifying carbon as the source of visible single-photon emission from hexagonal boron nitride. *Nat Mater* **2021**, *20*, 321–328.

58. Chejanovsky, N.; Mukherjee, A.; Geng, J.; Chen, Y.-C.; Kim, Y.; Denisenko, A.; Finkler, A.; Taniguchi, T.; Watanabe, K.; Dasari, D. B. R., *et al.* Single-spin resonance in a van der Waals embedded paramagnetic defect. *Nature Materials* **2021**, *20*, 1079–1084.

59. Stern, H. L.; Gu, Q.; Jarman, J.; Eizagirre Barker, S.; Mendelson, N.; Chugh, D.; Schott, S.; Tan, H. H.; Sirringhaus, H.; Aharonovich, I.; Atature, M. Room-temperature optically detected magnetic resonance of single defects in hexagonal boron nitride. *Nat Commun* **2022**, *13*, 618.